Science of the Total Environment 955 (2024) 176857

Contents lists available at ScienceDirect

Science of the Total Environment

journal homepage: www.elsevier.com/locate/scitotenv

A settling velocity formula for irregular shaped microplastic fragments based on new shape factor: Influence of secondary motions

Chaoqun Ji [a], Jinfeng Zhang [a,b], Guangwei Liu [a,*], Qinghe Zhang [a], Xiaoteng Shen [c]

[a] State Key Laboratory of Hydraulic Engineering Intelligent Construction and Operation, Tianjin University, Tianjin 300072, China
[b] Key Laboratory of Earthquake Engineering Simulation and Seismic Resilience of China Earthquake Administration, Tianjin University, Tianjin 300350, China
[c] The National Key Laboratory of Water Disaster Prevention, Hohai University, Nanjing, China

HIGHLIGHTS

- The secondary motion induced by shape influences the settling process.
- Microplastic fragments were classified into stable, transitional, and oscillating settling types.
- Presented irregular shape factor for irregular microplastic fragments.
- The presented formula for settling velocity shows better performance.

GRAPHICAL ABSTRACT

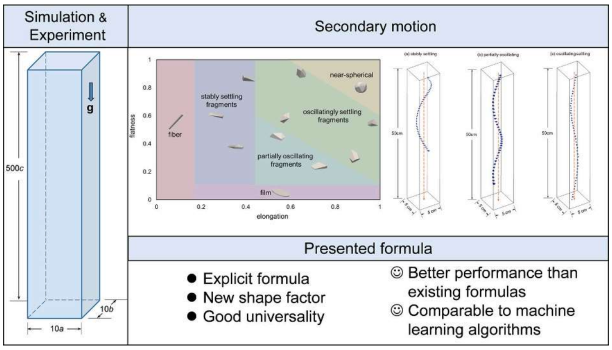

ARTICLE INFO

Editor: Thomas Kevin V

Keywords:
Microplastic fragments
Irregular shape
Terminal settling velocity
Shape factor
Drag coefficient

ABSTRACT

Microplastic (MP) fragments are prevalent in rivers and lakes and cause considerable pollution in natural water environments. Determining the settling velocity of microplastic fragments is crucial for predicting their migration and fate in aquatic systems. Predicting the settling velocity of MP fragments is challenging because of their complex and variable geometries and the uncertainties associated with secondary motions. To better understand the secondary motions of irregular MP fragments, a numerical model was developed to study the entire settling process, and an experiment was conducted to validate the numerical model. The model results showed the temporal changes in the settling velocity and orientation of MP fragments during the settling process. The MP fragments were classified according to their shape factors into fragments undergoing stable, transitional, and oscillating settling on the basis of velocity fluctuations caused by secondary motions. To describe the shape of irregular MP fragments appropriately, a new irregular shape factor (*ISF*) was derived by performing a theoretical analysis of forces and demonstrated to be more suitable than the Corey shape factor (*CSF*) for irregular MP fragments exhibiting considerable secondary motions. The settling velocity data were fitted to obtain an explicit settling velocity formula that includes the *ISF* for irregular MP fragments. Compared with machine learning methods and existing formulas, the proposed formula provides more accurate predictions of the settling velocity for irregular MP fragments.

---

* Corresponding author.
E-mail address: guangweiliu@tju.edu.cn (G. Liu).

https://doi.org/10.1016/j.scitotenv.2024.176857
Received 28 July 2024; Received in revised form 8 October 2024; Accepted 9 October 2024

1. Introduction

With the widespread production and extensive use of plastic products, environmental pollution caused by microplastics has become increasingly severe. In recent years, microplastics have been widely studied both in industry and the academic community. Microplastics account for a considerable portion of marine debris, where ocean litter has been reported to consist of >60 % plastic products (Ryan, 2015).

It is critical to investigate the migration of MP fragments to characterize their physical and biochemical hazards. During migration, microplastics are subjected to various environmental loads, including water flow, waves, surface tension, wind pressure, turbulence, and biochemical interactions. These factors result in a range of movement behaviors, such as convective translation and a turbulent random walk (Shamskhany and Karimpour, 2022),floating (Isobe et al., 2014; Iwasaki et al., 2017), wave-driven mass transport (DiBenedetto et al., 2019; Larsen et al., 2023; Lenain et al., 2019), settling (Choi et al., 2022; Jalon-Rojas et al., 2022; Qian et al., 2024; Van Melkebeke et al., 2020; Waldschlager and Schuttrumpf, 2019), flocculation (Laursen et al., 2022; Maliwan et al., 2021), stranding and resuspension (Moreira et al., 2016; Xue et al., 2020), and biofouling (Fazey and Ryan, 2016; Koelmans et al., 2016; Kooi et al., 2017). Besides, it is important to consider the accelerating effect of suspended sediment on the settling velocity of MPs in estuaries with low energy and high suspended sediment concentration (Mancini et al., 2023). Among them, the settling process of microplastics is one of the main factors affecting their migration (Jalon-Rojas et al., 2019). The settling velocity determines the residence time of microplastics in the water column, thereby influencing their migration paths and fate.

The physical properties of particles, such as the particle size, density, and shape, affect the settling velocity. The complex and various surface morphologies of microplastic particles have made traditional settling velocity models inadequate for predicting the settling velocity of microplastics (Khatmullina and Isachenko, 2017; Kooi et al., 2017; Van Melkebeke et al., 2020; Waldschlager and Schuttrumpf, 2019). Therefore, constructing a settling velocity model for microplastics requires accurately describing the particle shapes.

In addition to the properties of the microplastics, secondary motion affects the settling velocity. Secondary motion has been demonstrated to produce an additional lift force on MPs that affects their settling orientation and velocity (Zastawny et al., 2012). The settling velocity of MP fibers has been demonstrated to be influenced by secondary motion (Choi et al., 2022). The secondary motion of the MP fragments was reported to cause oscillations and horizontal movement (Waldschlager and Schuttrumpf, 2019) but oscillations in the velocity induced by secondary motion were not studied. Secondary motion transforms one-dimensional (vertical) settling motion into complex three-dimensional motion. Generally, secondary motion arises from shape-induced rotation and turbulence associated with high Reynolds numbers. However, owing to the small size and low density of microplastics, the settling motions of microplastics mainly fall within the laminar and transitional flow regimes (Yu et al., 2022), indicating that turbulence does not dominate MP settling. Nevertheless, the irregular and complex geometries of MP fragments introduce considerable secondary motion into the settling process (Waldschlager and Schuttrumpf, 2019). The asymmetric and irregular shapes of these fragments result in asymmetric forces, leading to horizontal and vertical movements that are difficult to predict. Therefore, formulas for the settling velocity of microplastics derived mainly from data on regular particles (e.g., fibers, cylinders, films, cubes and pellets) may underestimate the impact of secondary motion on the settling velocity. A key challenge in studying the secondary motion of irregular MP fragments experimentally is the difficulty of capturing their dynamic and instantaneous movements. Imaging equipment with a wide field of view must be used to capture the overall settling path (Choi et al., 2022), whereas tracking the instantaneous velocity requires the use of a technology with a high resolution and small field of view, such as PIV (particle image velocimetry) (Waldschlager and Schuttrumpf, 2019). In Section 4.1 Secondary motion, the results of both numerical simulations and experiments are presented to show the impact of secondary motion on the settling velocity of irregular MP fragments.

Existing formulas for the settling velocity of regular microplastics with various shapes have been shown to have excellent predictive ability. Formulas have been developed (Wang et al., 2021) for the settling velocity of microplastics under both static and dynamic water conditions but are not dimensionally consistent because the predicted settling velocity does not have units of length per time $[L/T]$. The settling velocity has been measured experimentally for only eight irregular particles (Goral et al., 2023).

In addition to experiments, mathematical models are also a means of studying the settling velocity of microplastics. A fully analytical three-dimensional numerical model has been used to simulate the complete settling process of microplastic particles (Zhang et al., 2023). In this study, a fully analytical numerical model was used to simulate the settling processes of MP fragments to obtain settling velocity data. The temporal settling velocities were analyzed to determine the impact of secondary motion on the settling of irregular MP fragments. A settling velocity formula containing the *ISF* was developed for irregular MP fragments.

Physical static water settling experiments were conducted on 3D printed millimeter-scale irregular MP fragments. The experimentally measured settling velocities were used to validate the developed formula.

Section 2 provides a brief overview of the development of the settling velocity problem of MPs. The properties of the irregular MP fragments and the setup of the numerical model and experiment are detailed in Section 3. In Section 4, the secondary motion was analyzed, and an irregular shape factor and a settling velocity formula were presented. Finally, in Section 5, conclusions were presented and the limitations of the study and future work was discussed.

2. Theoretical background

The settling velocities of different types of microplastics have been investigated in previous studies (Table 1). The formulas presented in the table correspond to different shapes, such as pellets (Chubarenko et al., 2016; Francalanci et al., 2021; Khatmullina and Isachenko, 2017; Kowalski et al., 2016), cylinders (Khatmullina and Isachenko, 2017; Kowalski et al., 2016; Waldschlager and Schuttrumpf, 2019; Zhang et al., 2023), fibers (Chubarenko et al., 2016; Jalon-Rojas et al., 2022; Khatmullina and Chubarenko, 2021; Khatmullina and Isachenko, 2017; Nguyen et al., 2022; Van Melkebeke et al., 2020; Waldschlager and Schuttrumpf, 2019; Zhang and Choi, 2022), films (Jalon-Rojas et al., 2022; Ji et al., 2024), and granules (Francalanci et al., 2021; Goral et al., 2023; Kowalski et al., 2016; Van Melkebeke et al., 2020; Waldschlager and Schuttrumpf, 2019; Wang et al., 2021). According to whether the specific morphology (volume, surface area, particle size, *CSF*, etc.) of the particles can be determined by the axes *a*, *b* and *c*, MPs studied in the existing research can be divided as regular (Chubarenko et al., 2016; Francalanci et al., 2021; Goral et al., 2023; Jalon-Rojas et al., 2022; Ji et al., 2024; Khatmullina and Isachenko, 2017; Kowalski et al., 2016; Nguyen et al., 2022; Van Melkebeke et al., 2020; Waldschlager and Schuttrumpf, 2019; Yu et al., 2022; Zhang and Choi, 2022) and irregular (Francalanci et al., 2021; Goral et al., 2023; Kowalski et al., 2016; Waldschlager and Schuttrumpf, 2019; Yu et al., 2022). Fragments have been reported to account for 2.5 % ~ 48 % of microplastics in natural water environments (Gray et al., 2018; Song et al., 2014; Yan et al., 2019).

The settling velocity of microplastics is typically predicted using formulas. Empirical formulas are often derived from settling experimental data for one or more types of regular microplastic particles. However, few studies have been performed on particles with 3D irregular shapes, and the results of studies on regular particles may not be suitable for predicting the settling behavior of irregular MP fragments exhibiting secondary motion. Unlike determining the settling velocity for regular particles, accurately determining the settling velocity of irregular microplastic particles requires the selection of an appropriate shape factor. The Corey shape factor *CSF* is commonly used in settling velocity formulas for microplastics:

$$CSF = \frac{c}{\sqrt{ab}} \tag{1}$$

where *a*, *b* and *c* represent the longest, intermediate and shortest oriented particle axes of a bounding box, respectively. Other shape factors, such as the sphericity Ψ, flatness *f*, elongation *e* and Aschenbrenner shape factor (*ASF*), are also used in settling velocity formulas to account for the different shapes of microplastics:

$$\psi = S_s/S \tag{2}$$

$$f = c/b \tag{3}$$

$$e = b/a \tag{4}$$

$$ASF = ac/b^2 \tag{5}$$

where S_s and S are the surface areas of an equivalent-volume sphere and the particle itself, respectively. The shape factors that have been used in studies on the settling velocities of MPs are listed in Table 1. The *CSF* equals the size of a bounding box of a particle, such that particles with different shapes can have the same *CSF*. Therefore, characterizing the shapes of irregular particles and predicting their settling velocities remain challenging. Fig. 1 shows that two different particles with the same diameter D_n of the equivalent-volume sphere, particle density ρ_p and *CSF* have different drag areas, which implies that different drag forces may be exerted on these particles. However, settling velocity formulas containing the *CSF* are based on the assumption that the settling velocity is a univocal function of D_n, ρ_p and *CSF*, which may be unphysical. In Section 4.2, we provide a theoretical explanation for why the *CSF* is not an appropriate shape factor for irregular MP fragments and propose a new irregular shape factor (*ISF*).

3. Materials and methods

3.1. Properties of the irregular MP fragments

Irregular particles can be generated by the Boolean operation (Wu et al., 2022), Monte Carlo (Wang et al., 2020; Zou et al., 2007), and fractal geometry methods (Zhou et al., 2023). In this study, the fractal geometry method is used to generate irregular microplastics via artificial planar cutting for both experiments and simulations. A microplastic cube with a side length of 5 mm is cut into multiple random planes to ensure that the particle size is <5 mm and meets the criteria for microplastics, resulting in millimeter-scale irregular MP fragments.

The properties of the irregular MP fragments used in both the physical experiments and numerical simulations are detailed in the Supplementary Data. Both the experimental and simulated microplastics are asymmetrical and irregular in shape. On the basis of two classification methods (see (Qian et al., 2024) and (Choi et al., 2022)), microplastic particles with an elongation $e > 0.2$ and flatness $f > 0.1$ are considered MP fragments. A variety of shapes with a wide distribution was needed to ensure that the selected irregular microplastics were representative MP fragments. Fig. 2 shows the 20 shapes of MP fragments that were systematically selected for this study on the basis of the shape factors *e* and *f*.

Simulations were performed on MP fragments made of Polystyrene (PS, 1.04 g/cm^3), Polycaprolactone (PCL, 1.13 g/cm^3) and Polyvinyl chloride (PVC, 1.35 g/cm^3) to cover the density range of most negatively buoyant microplastics. The size of the MP fragments was varied to generate a total of 120 irregular MP fragments, which distinguished by their sizes, diameters, and densities. The overall distributions of the MP characteristics are shown in Fig. 3.

Experiments were performed on ten MP fragments made of resin. The properties of the MP parameters are given in Table 2 and the infrared spectrogram of the resin is provided in the Supplementary material to help characterize the material.

3.2. Numerical model

In this study, a numerical model for static water settling is constructed using the lattice Boltzmann and immersed boundary methods. The coupled model can be used to precisely characterize particles with complex shapes and realize bidirectional coupling of fluids and solids in real time. The motion of the particles is solved according to Newton's second law, and physical quantities related to translation and rotation are calculated. The ability of an IB-LBM to simulate the sedimentation of microplastics has previously been demonstrated (Ji et al., 2024; Zhang et al., 2023).

The flow field is simulated by lattice Boltzmann method. The multi-relaxation time (MRT) lattice Boltzmann equation (Lallemand et al., 2021) can be expressed as:

$$f_\alpha(\mathbf{x} + \mathbf{e}_\alpha \Delta_t, t + \Delta_t) - f_\alpha(\mathbf{x}, t) = \mathbf{M}^{-1}\mathbf{S}\mathbf{M}[f_\alpha(\mathbf{x}, t) - f_\alpha{}^{eq}(\mathbf{x}, t)] + O(\Delta_t{}^2) \tag{6}$$

where $f_\alpha(\mathbf{x} + \mathbf{e}_\alpha \delta_t, t + \delta_t)$ and $f_\alpha(\mathbf{x}, t)$ are the distribution functions before and after the process of collision and stream, respectively; $\mathbf{M}^{-1}\mathbf{S}\mathbf{M}$ is the multi-relaxation parameter matrix; Δ_t is the lattice unit time; and $f_\alpha^{eq}(\mathbf{x}, t)$ is the equilibrium distribution function. As regard incompressible flows, the Incompressible equilibrium distribution function can be obtained:

Table 1
Studies on determining the settling velocity of microplastics.

Reference	Pellet	Cylinder	Fiber	Film	Granular	Regular	Irregular	Shape factor	Presented formula for various shaped MPs
(Chubarenko et al., 2016)	✓		✓			✓			
(Kowalski et al., 2016)	✓	✓			✓	✓	3D Irregular		
(Khatmullina and Isachenko, 2017)	✓	✓	✓			✓		L/D	
(Waldschlager and Schuttrumpf, 2019)		✓			✓	✓	3D Irregular	CSF	✓
(Van Melkebeke et al., 2020)			✓		✓	✓		Ψ	
(Francalanci et al., 2021)	✓				✓	✓	2D Irregular	CSF	✓
(Khatmullina and Chubarenko, 2021)			✓					CSF	
(Jalon-Rojas et al., 2022)			✓	✓		✓		Ψ	
(Nguyen et al., 2022)			✓			✓			
(Zhang and Choi, 2022)			✓			✓		ASF	
(Yu et al., 2022)							3D Irregular	CSF, Ψ	✓
(Goral et al., 2023)					✓	✓	3D Irregular	Ψ	✓
(Ji et al., 2024)				✓		✓		f	

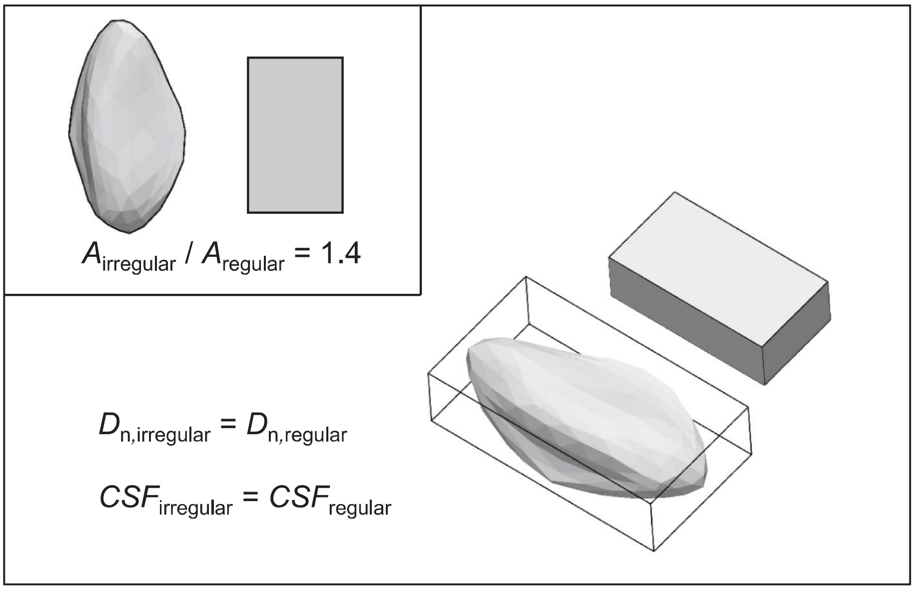

Fig. 1. Regular and irregular MP fragments with the same D_n and *CSF*. The drag areas are shown in the upper left portion of the figure.

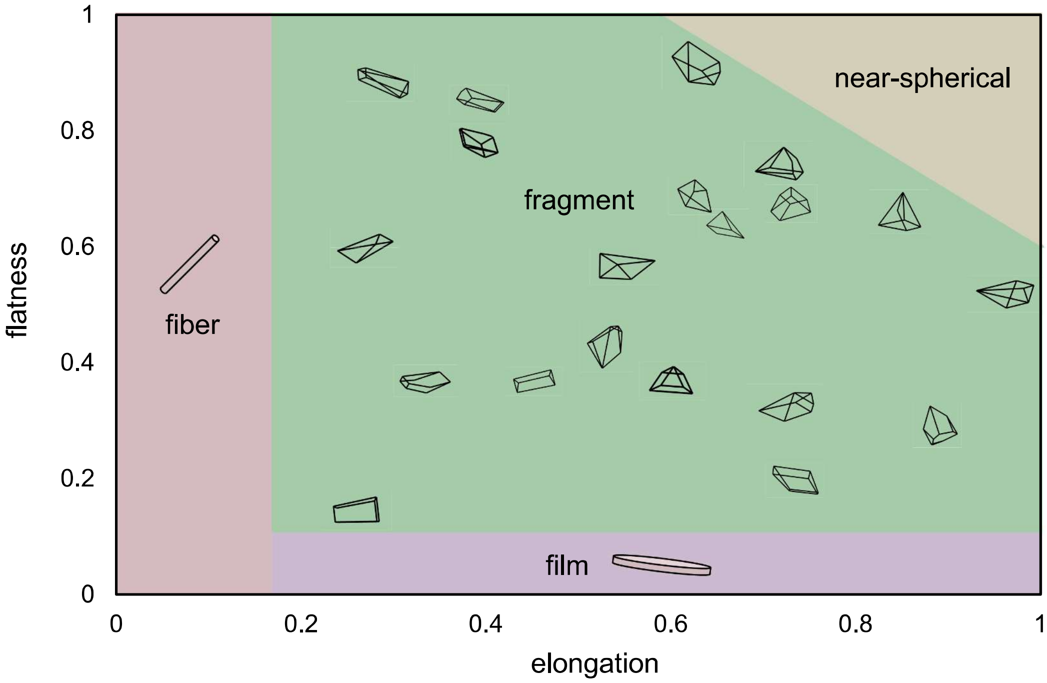

Fig. 2. Shape distribution of the selected irregular MP fragments.

$$f_\alpha^{eq} = t_\alpha\rho + t_\alpha\rho_0\left[\frac{\mathbf{e}_\alpha\cdot\mathbf{u}(\mathbf{x},t)}{c_s^2} + \frac{(\mathbf{e}_\alpha\cdot\mathbf{u}(\mathbf{x},t))^2}{2c_s^4} - \frac{|\mathbf{u}(\mathbf{x},t)|^2}{2c_s^2}\right] \tag{7}$$

where t_α is the streaming weight coefficient. In the D3Q27 model, $t_0 = 8/27$,$t_{1-6} = 2/27$, $t_{7-18} = 1/54$, and $t_{19-26} = 1/216$. Moreover, $\mathbf{e}_\alpha$ is the discrete lattice velocity; and $\mathbf{u}(\mathbf{x}, t)$ is the macroscopic Euler velocity. Based on the Chapman-Enskog expansion, the incompressible lattice Boltzmann equation can be transformed to the macroscopic incompressible Navier – Stokes equation:

$$\nabla\cdot\mathbf{u}(x,t) = O\left(\text{Ma}^2\right) \tag{8}$$

$$\frac{\partial\mathbf{u}(\mathbf{x},t)}{\partial t} + \mathbf{u}(\mathbf{x},t)\cdot\nabla\mathbf{u}(\mathbf{x},t) = -\frac{\nabla p(\mathbf{x},t)}{\rho_0} + \nu\nabla^2(\mathbf{u}(\mathbf{x},t)) + O\left(\text{Ma}^3\right) \tag{9}$$

where $\mathbf{u}(\mathbf{x},t)$, $p(\mathbf{x},t)$, and ν are the flow velocity, pressure and viscosity, respectively. Under the constraint of a small Mach number ($Ma < 0.15$), the LBM achieves second-order temporal and spatial accuracy.

$$\sum_{\alpha=1}^{q} f_\alpha(\mathbf{x},t) = \sum_{\alpha=1}^{q} f_\alpha^{eq}(\mathbf{x},t) = \rho \tag{10}$$

$$\sum_{\alpha=1}^{q} \mathbf{e}_\alpha f_\alpha(\mathbf{x},t) = \sum_{\alpha=1}^{q} \mathbf{e}_\alpha f_\alpha^{eq}(\mathbf{x},t) = \rho_0\mathbf{u} \tag{11}$$

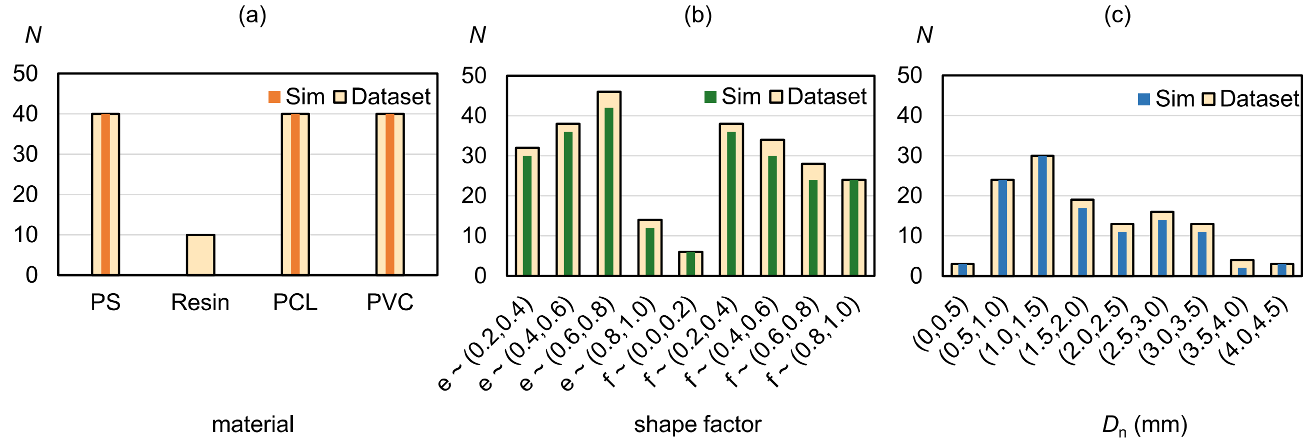

Fig. 3. Distributions of the characteristics of the irregular MP fragments: (a) material, (b) shape factor, and (c) D_n.

Table 2
Properties of MP Fragments Used for Experiments.

Number	D_n (cm)	Density (g/cm^3)	e	f
1	0.08	1.20	0.98	0.55
2	0.12	1.20	0.68	0.92
3	0.12	1.20	0.57	0.59
4	0.06	1.20	0.28	0.60
5	0.10	1.20	0.76	0.22
6	0.20	1.20	0.98	0.55
7	0.31	1.20	0.68	0.92
8	0.31	1.20	0.57	0.59
9	0.15	1.20	0.28	0.60
10	0.26	1.20	0.76	0.22

where q is the total number of discrete directions in the lattice space.

The force exerted on the particles is calculated by IBM (immersed boundary method) by measuring the difference between the velocity of control points at the particle boundary and the fluid velocity $\mathbf{u}(\mathbf{X}_k^b, t+\Delta t)$, which is obtained by interpolating the velocity of surrounding Euler points:

$$\mathbf{u}(\mathbf{X}_k^b, t+\Delta t) = \sum_{\mathbf{x}} \mathbf{u}(\mathbf{x}, t+\Delta t) W(\mathbf{x}-\mathbf{X}_k^b)(\Delta x)^d \tag{12}$$

where $\sum_{\mathbf{x}}$ describes the sum of all Eulerian points and d is the dimension. W is the weight coefficient for interpolation and extrapolation, determined by the relative position of the i-th Euler point and the j-th Lagrangian point:

$$W_{ij}(t) = \frac{1}{\Delta x}\delta\left(\frac{x_i - X_j(t)}{\Delta x}\right)\cdot\frac{1}{\Delta x}\delta\left(\frac{y_i - Y_j(t)}{\Delta x}\right)\cdot\frac{1}{\Delta x}\delta\left(\frac{z_i - Z_j(t)}{\Delta x}\right) \tag{13}$$

where δ is the regular trigonometric function.

The interaction between MP fragments and water is achieved by coupling IBM and LBM. IBM corrects the velocity of the fluid at the particle boundary position to be equal to the velocity of the object boundary, and the difference in velocity before and after correction is proportional to the magnitude of the immersed boundary force density:

$$\Delta\mathbf{g}(\mathbf{X}_k^b, t+\Delta t) = \rho\frac{\mathbf{U}_k^b - \mathbf{u}(\mathbf{X}_k^b, t+\Delta t)}{\Delta t} \tag{14}$$

The fluid forces acting on the Lagrange points can be expressed as follows:

$$\mathbf{g}(\mathbf{X}_k^b, t+\Delta t) = \mathbf{g}(\mathbf{X}_k^b, t+\Delta t) + \Delta\mathbf{g}(\mathbf{X}_k^b, t+\Delta t) \tag{15}$$

The force acting on the Euler point can be extrapolated from the IBM force layer:

$$\mathbf{g}(\mathbf{x}, t+\Delta t) = \sum_{k=1}^{N}\mathbf{g}(\mathbf{X}_k^b, t+\Delta t) W(\mathbf{x}-\mathbf{X}_k^b)\Delta V_i \tag{16}$$

The distribution function of Euler points $f(\mathbf{x}, t+\Delta t)$ is modified using the second-order discrete scheme of force proposed by (Guo et al., 2002):

$$f(\mathbf{x}, t+\Delta t) = f(\mathbf{x}, t+\Delta t) + \left(1-\frac{1}{2\tau}\right)t_\alpha\left(\frac{\mathbf{e}_\alpha - \mathbf{u}}{c_s^2} + \frac{(\mathbf{e}_\alpha\cdot\mathbf{u})}{c_s^4}\mathbf{e}_i\right)\cdot\mathbf{g}(\mathbf{x}, t) \tag{17}$$

where τ is the relaxation time. The Euler point modifies its temporary Eulerian velocity $\mathbf{u}^*(\mathbf{x}, t+\Delta t)$ as follows:

$$\mathbf{u}(\mathbf{x}, t+\Delta t) = \mathbf{u}^*(\mathbf{x}, t+\Delta t) + \Delta t\mathbf{g}(\mathbf{x}, t+\Delta t) \tag{18}$$

The dimensions of the numerical model were $500c$ (height) × $10a$ × $10a$. The MP fragments were initially placed at the horizontal center of the model, and the distance between the center of the fragments and the upper wall was set at $50c$ to reduce the numerical instability caused by oscillations near the boundary. For particles with different sizes ($a/b/c$), the actual size of the computational domain varies according to the particle size. The practice of dynamically changing the size of the computational domain is to avoid unnecessary computational consumption. The lattice size of the uniform grid dx was $D_n/15$, and the corresponding number of lattices was O (10^8). Periodic vertical boundaries were used for the numerical model of the settling cylinder and the IBM algorithm to meet the lattice requirement for the horizontal translation of MP fragments. Multiple processors were run in parallel at the National Supercomputing Center in Tianjin, China to conduct the simulation.

A lattice sensitivity analysis was performed to ensure that the lattice size dx was sufficiently fine and that the calculation of the terminal settling velocity was not affected by the grid size. The simulation was performed on an irregular MP fragment made of PVC with $D_n = 0.41$ cm because of its large D_n and high Reynolds number, which usually require a finer grid. A comparative analysis was conducted on four different grid sizes, $D_n/9$, $D_n/12$, $D_n/15$, and $D_n/18$, and the resulting settling velocities are shown in Table 3. Similar results were obtained using $dx = D_n/15$ and $dx = D_n/18$, with a relative error of 2.2 %, basically meeting the grid size requirements (Fig. 4).

3.3. Experiment setup

A settling experiment was conducted at the State Key Laboratory of Hydraulic Engineering Intelligent Construction and Operation of Tianjin University. The settling column had dimensions of 70 cm (height) × 15 cm × 15 cm. Under the laboratory conditions, the water had a temperature of 20 °C, $\rho = 0.998$ g/cm^3 and $\nu = 10^{-2}$ cm^2/s. To ensure that

Table 3
Lattice sensitivity analysis.

Lattice size *dx*	$D_n/9$	$D_n/12$	$D_n/15$	$D_n/18$
Settling velocity (cm/s)	9.98	10.40	10.68	10.91
Relative error (%)	8.5	4.7	2.2	/

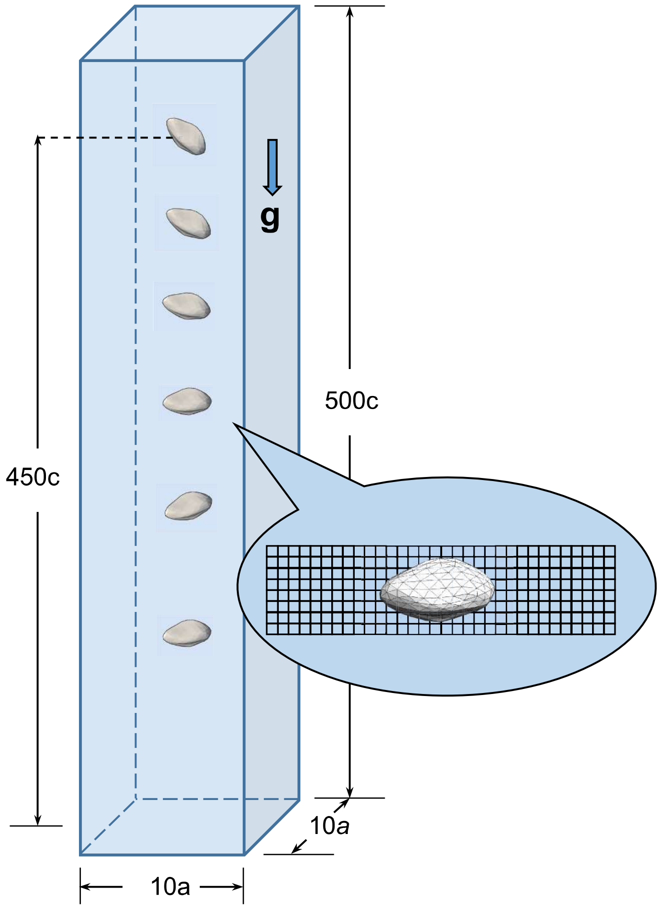

Fig. 4. The simulation domain for an irregular MP fragment settling in quiescent water.

the settling process was not affected by surface tension, the MP fragments were initially placed approximately 2 cm below the water surface. A light source lamp, with a maximum luminous flux of 25,000 lm and an average illuminance of 572,000 1×, is placed on the side of the settling column at an angle of approximately 90° to the direction of the camera to ensure that the fragments were visible during the settling process. A black curtain is placed behind the settling column to enhance the contrast between the particles and the background. The settling process was observed using a camera that could automatically record the displacement and calculate the velocity. The frequency was set to 25 frames per second, and the exposure time was 10,000 us. Refer to the operation of (Choi et al., 2022), who studied the secondary motion of MP fibers on the settling velocity, the measurements are started when the fragment is 70 mm beneath the water surface. Only one MP fragment was tested in each experiment to avoid the influence of the mutual flow field and unwanted collisions caused by multi-particle settling on the settling velocity. For each particle, take the average value of three repeated experiments as the settling velocity. The experimental setup is shown in Fig. 5.

4. Results and discussion

4.1. Secondary motion

The orientation and velocity of MP fragments change during settling. Fig. 6 shows the temporal variation in the settling velocity. The one-dimensional MP fragments shown in Fig. 6(a)–(c), whose longest axes are significantly longer than the intermediate and shortest axes, exhibit stable settling, which is not sensitive to the particle density. The stable particle orientation results in the fragments maintaining a stable terminal settling velocity. The MP fragments shown in Fig. 6(f)–(i), whose longest, intermediate and shortest axes are close, exhibit oscillating settling. The settling velocity oscillates harmonically, maintaining the same period and amplitude with fluctuations around the terminal value. The MP fragments undergo secondary motion at a constant frequency and amplitude, but the oscillation trend does not converge. The transitional MP fragments shown in Fig. 6(d) and (e) have similar shapes to films whose longest and intermediate axes are significantly longer than the shortest axes. The velocity of the transitional MP fragments is sensitive to the density, converging at low densities and oscillating at high densities.

The relationship between the secondary motions of settling motion and the shape properties of MP fragments was used to classify the secondary motion of MP fragments into stable, transitional or oscillating settling, as shown in Fig. 7.

The following results were obtained from the numerical model for the particle orientation during settling: unlike regular shapes, such as fibers (Zhang et al., 2023), some irregular particles do not converge to the maximum settling surface during the settling process but instead undergo oscillating rotation around the maximum projection. Fig. 8 shows the changes in particle orientation between the stably settling particle and the oscillating settling particle. The orientation of the fragments undergoing stable settling changes slowly, resulting in minimal secondary motion and rotational amplitude, such that the maximum projection area generally remains perpendicular to the settling direction. By contrast, the fragments undergoing oscillating settling change position dramatically, accompanied by large rotational amplitudes and horizontal displacements. The fragments undergoing oscillating settling typically have higher Reynolds (4.04–398.7) numbers than non-oscillating fragments (0.99–206.74), increasing the susceptibility of their settling velocities to turbulence (see the vorticity map shown in Fig. 8). The vorticity is calculated as the reciprocal of velocity:

$$\boldsymbol{\omega} = \nabla \times \mathbf{u} \tag{19}$$

Increasing turbulence could potentially intensify secondary motion. By comparison, less turbulence is generated during stable settling.

The asymmetry of the irregular MP fragments results in imbalances in the bending moments and forces exerted on the fragments, resulting in rotation of the fragments that induces secondary motion in both the horizontal and vertical directions. The fragments exhibit oscillating motion, and secondary motion leads to horizontal displacement, as shown in Fig. 9. Fig. 9(a) shows MP fragments undergoing stable settling that exhibit regular circular motion, whereas the fragments undergoing oscillating settling shown in Fig. 9(c) have an irregular and wavy circular trajectory.

The trajectory of the irregular MP particle undergoing settling is shown in Fig. 10. The orientation of irregular MP fragments is similar to a previously defined spiral state (Zhong et al., 2011). The irregular shapes and asymmetric forces exerted on the MP fragments result in horizontal motion. The MP fragments oscillate horizontally and periodically around a certain vertical axis, while the angle between the fragments and the vertical axis changes continuously. Although the settling velocity of the MP fragments undergoing stable settling is almost unaffected by secondary motion, the horizontal displacement of these fragments is larger than those undergoing transitional or oscillating settling. This finding aligns with the experimental results showing that

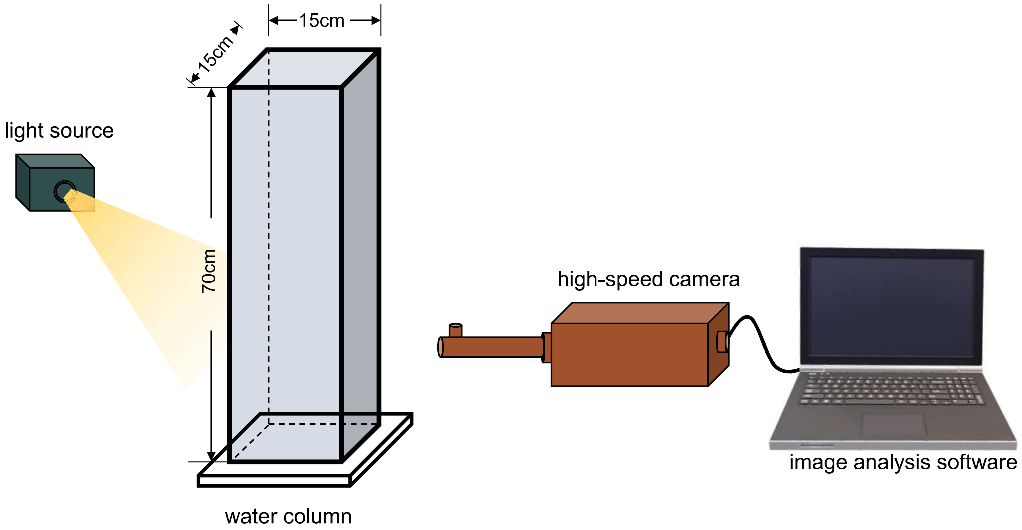

Fig. 5. Setup for the settling experiment.

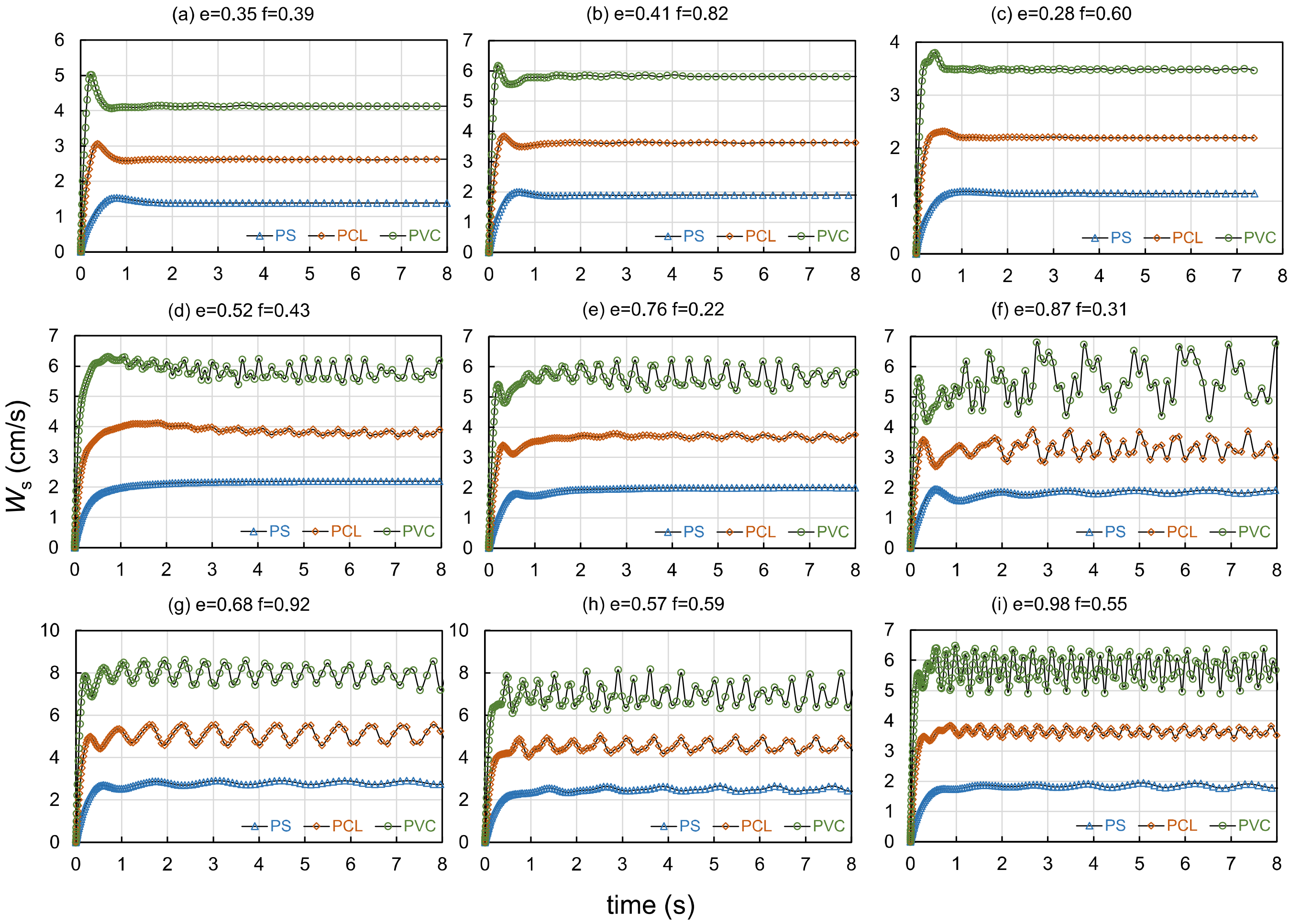

Fig. 6. Duration curve of the settling velocity of irregular MP fragments.

the most elongated fragments (the particles with the smallest elongation *e*) scatter farthest (Choi et al., 2022).

Analysis of the secondary motion of the irregular MP fragments revealed that although the fragment orientation changes during the settling process, the fragment velocity fluctuates regularly around the terminal value once settling stabilizes. The MP fragments undergoing stable settling have a constant terminal velocity. For the fragments undergoing oscillating and transitional settling, the terminal settling velocity is taken as the average settling velocity during a period of “stable oscillation.” The terminal settling velocities are presented in Section 4.3.

Fig. 11 shows the trajectory of the MP fragments during the settling experiment. Consistent with the results of the numerical model, the

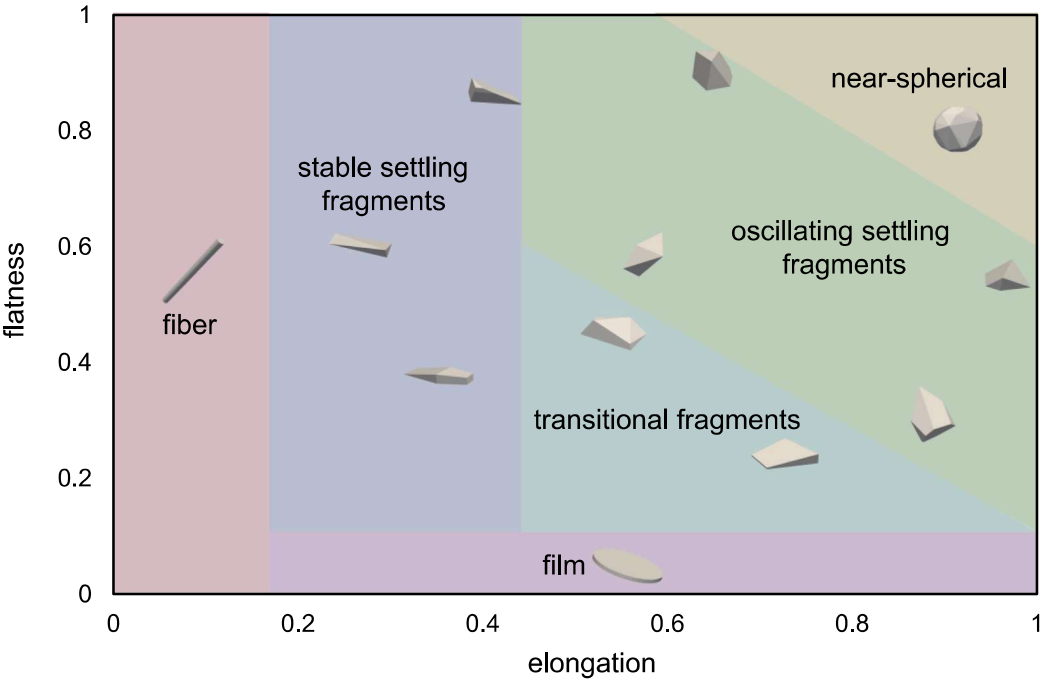

Fig. 7. Classification of the secondary motion of irregular MP fragments.

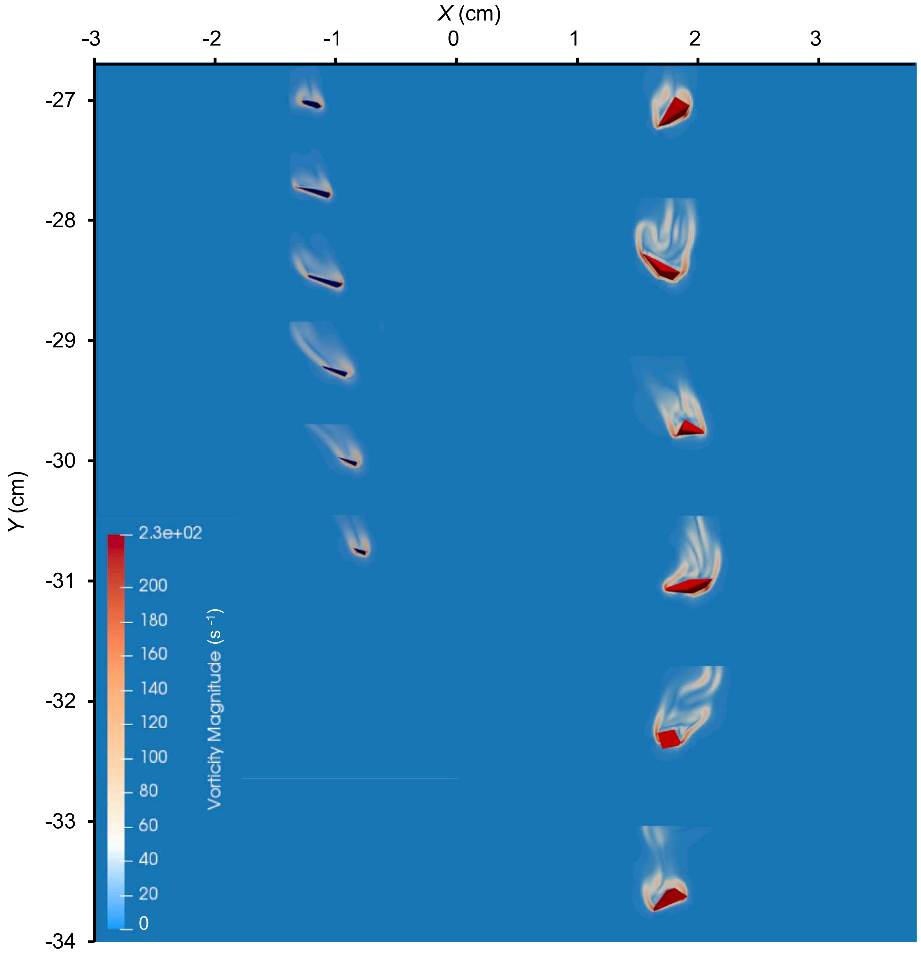

Fig. 8. Settling orientation and vorticity map of the instantaneous flow field of irregular MP fragments. The blue MP fragment on the left, with $e = 0.28$ and $f = 0.60$, undergoes stable settling, whereas the red MP fragment on the right, with $e = 0.57$ and $f = 0.59$, undergoes oscillating settling.

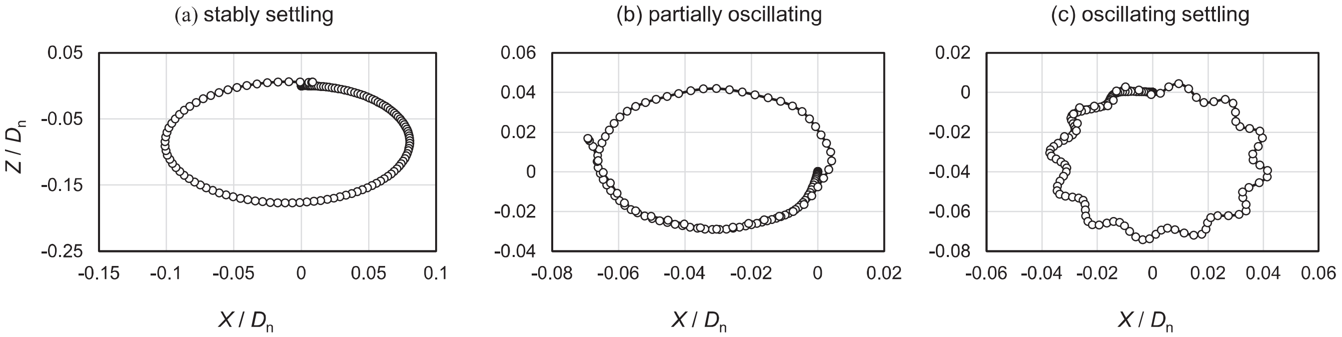

Fig. 9. Top view of horizontal displacement during the settling process. (a) a fragment with $e = 0.35$ and $f = 0.39$ undergoing stable settling; (b) a fragment with $e = 0.76$ and $f = 0.22$ undergoing transitional settling; and (c) a fragment with $e = 0.98$ and $f = 0.55$ undergoing oscillating settling. The uppercase letters *X* and *Z* represent the Cartesian axis in the horizontal plane. The *X*-axis is parallel to the long axis *a* of the particle, and the *Z*-axis is parallel to the intermediate axis *b* of the particle.

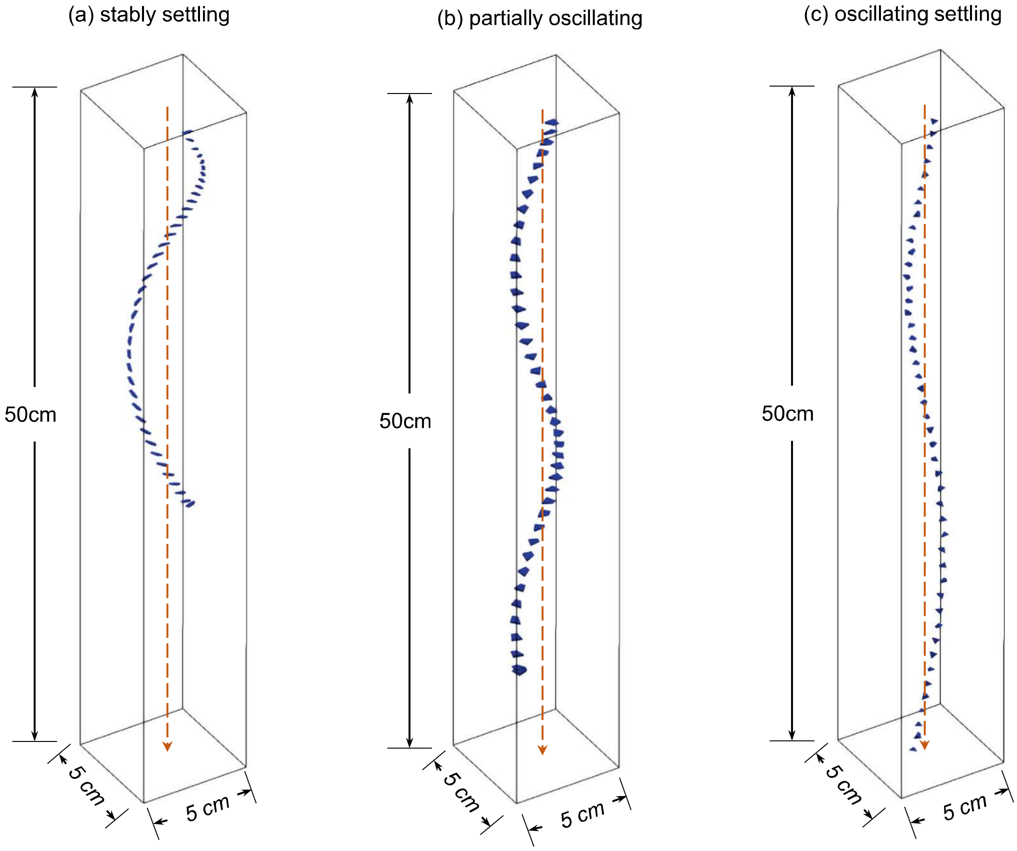

Fig. 10. Trajectories and orientations of three types of MP fragments: (a) a fragment with $e = 0.35$ and $f = 0.39$ undergoing stable settling; (b) a fragment with $e = 0.76$ and $f = 0.22$ undergoing transitional settling; and (c) a fragment with $e = 0.57$ and $f = 0.59$ undergoing oscillating settling.

transitional MP fragment (Fig. 11a) has larger horizontal displacement, whereas the settling velocity of the MP fragment undergoing oscillating settling (Fig. 11b) has larger oscillation amplitude.

4.2. A new shape factor for irregular shaped MP fragments

As previously discussed, it is difficult to use the *CSF* based on a bounding box to fully represent the shape of irregular MP fragments. On the basis of the analysis presented in Section 4.1, the settling orientations of irregular MP fragments converge to or oscillate around the maximum projection area, indicating that the maximum projection area is closely related to the settling velocity. In this section, we derive a new shape factor on the basis of the maximum projection area. According to Bernoulli's equation,

$$F_{CD} = 0.5\rho A C_D W_S^2 \tag{20}$$

where F_{CD} is the drag force, ρ is the fluid density, W_s is the terminal settling velocity, C_D is the drag force coefficient, and A is the maximum projection area. When the settling velocity stabilizes around the terminal value, the drag force and the net gravity of the object are dynamically balanced as follows:

$$\text{Irregular}: \int_{A_{\text{project}}} h(A)dA(\rho_p - \rho)g = 0.5\rho A_{\text{project}} C_D W_S^2 \tag{21}$$

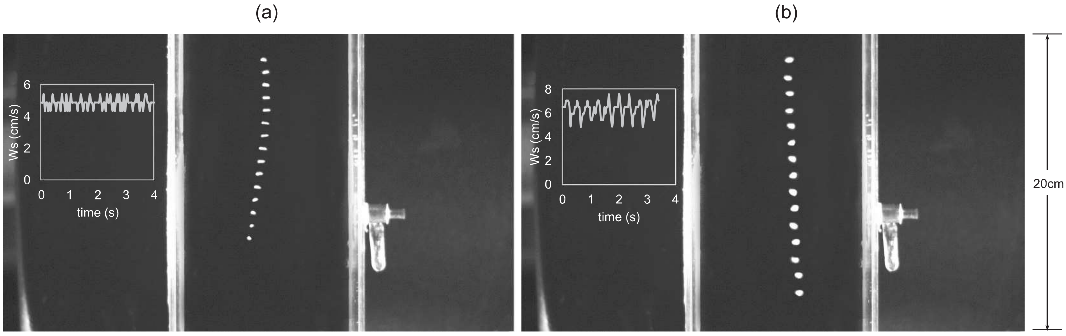

Fig. 11. The trajectory and velocity curve captured in the settling experiment on an MP fragment with (a) $e = 0.76$ and $f = 0.22$ and (b) $e = 0.57$ and $f = 0.59$.

$$\text{Regular}: V(\rho_p - \rho)g = 0.5\rho A C_D {W_S}^2 \tag{22}$$

where dA is the area element on the maximum projection plane, $\int dA = A$, $h(A)$ is the height of the fragment in the settling direction corresponding to dA expressed as a function of the projected area A and changes with dA for irregular MP fragments, and g (= 981 cm/s^2) is the acceleration due to gravity. According to Eqs. (21) and (22), C_D can be calculated as:

$$\text{Irregular}: C_D = \frac{2(\rho_p - \rho)g}{\rho A_{\text{project}} {W_S}^2} \int_{A_{\text{project}}} h(A)\text{dA} \tag{23}$$

$$\text{Regular}: C_D = \frac{2(\rho_p - \rho)g}{\rho A_{\text{project}} {W_S}^2} V \tag{24}$$

The only difference between the drag force coefficients of regular and irregular fragments is the shape factor; that is, the other characteristics (the density, particle size, etc.) can all be the same, corresponding to $\int h(A)\text{dA}$ in Eq. (23) and V in Eq. (24). To better describe the influence of the fragment shape on C_D, a dimensionless transformation is applied to $\int h(A)\text{dA}$ to make the shape factor independent of the fragment size. We have already explained why the size of a bounding box is an unsuitable shape factor; thus, we select the projection area A_{project}, which is directly related to the resistance to settling, to facilitate the dimensionless transformation. Thus Eqs. (23) and (24) are transformed into:

$$\text{Irregular}: C_D = \frac{2(\rho_p - \rho)g\sqrt{A_{\text{project}}}}{\rho {W_S}^2} \cdot \frac{\int_{A_{\text{project}}} h(A)dA}{(A_{\text{project}})^{3/2}} \tag{25}$$

$$\text{Regular}: C_D = \frac{2(\rho_p - \rho)g\sqrt{A_{\text{project}}}}{\rho {W_S}^2} \cdot \frac{c}{\sqrt{ab}} \tag{26}$$

So far, the latter term on the right side of Eqs. (25) and (26) are dimensionless. The second term for an irregular fragment reduces to $c/\sqrt{ab}$ for regular fragments and is commonly used as *CSF*. For irregular fragments, this term can be simplified to the ratio of the equivalent short-axis height h (= V/A_{project}) to the characteristic projection length $\sqrt{A_{\text{project}}}$. A new irregular shape factor, $ISF = h/\sqrt{A_{\text{project}}}$ is thus derived. The *ISF* and *CSF* are equivalent for regular microplastics.

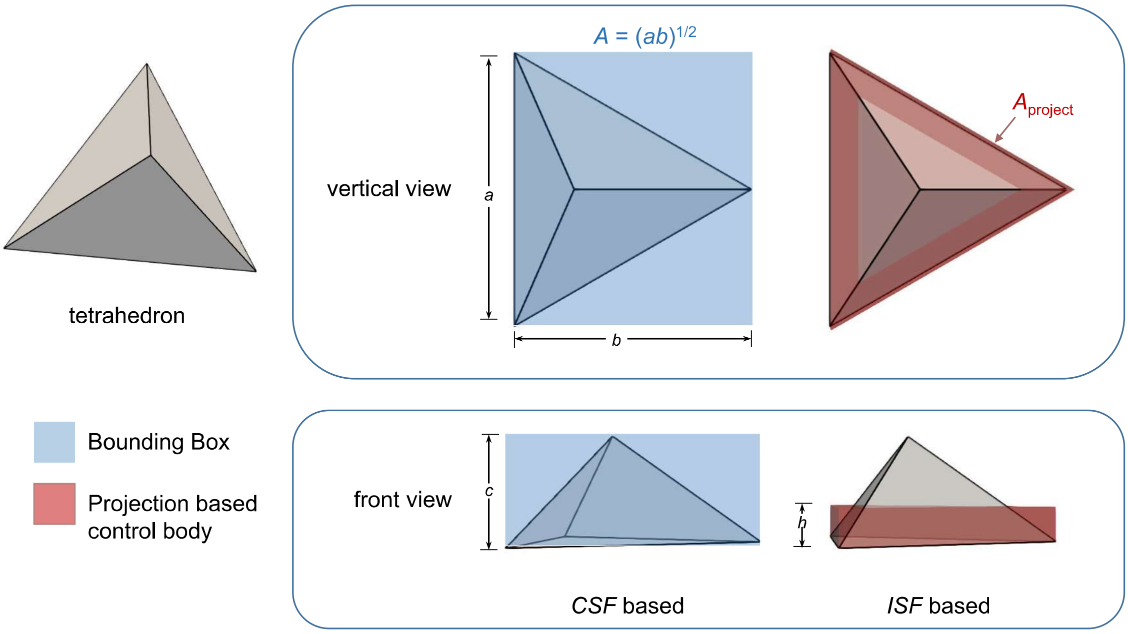

Fig. 12. The characteristic height and area of a tetrahedra defined by *CSF* and *ISF* respectively.

Fig. 12 uses a tetrahedron as an example to illustrate the difference between *ISF* and *CSF*, where the blue area represents the bounding box and the red area represents the projected control volume. The bounding box has a larger height *c* and area *A*. The maximum projection area A_{project} can be determined by using the Principal Component Analysis (PCA) algorithm provided in the Supplementary file.

In previous studies, the actual projected area of irregular particles was not reported; this area is required to calculate the proposed *ISF*, making it is difficult to demonstrate the effectiveness of the *ISF*. To demonstrate the effectiveness of the *ISF* and develop a suitable formula for the settling velocity, more data are needed on the settling velocities of irregular MP fragments. To demonstrate the advantage of using the *ISF* to predict the settling velocity for irregular MP fragments, a universal formula for the settling velocity of microplastics of various shapes, considering the largest number of microplastic particles, is used as a reference (Yu et al., 2022). Table 4 shows the results of the settling velocities from numerical simulation of irregular particles and equivalent regular rectangular particles (with the same size D_{n}, density ρ_{p}, and *CSF* as the irregular fragments), as well as the values predicted using the *CSF* and *ISF*. The MP fragment A with $e = 0.35$ and $f = 0.39$ undergoing stable settling, MP fragment B with $e = 0.52$ and $f = 0.43$ undergoing transitional settling and MP fragment C with $e = 0.87$ and $f = 0.31$ undergoing oscillating settling were selected to perform a comparative analysis. First, for the equivalent regular MP fragments, both the numerical models and formulas accurately predict the settling velocity with errors ranging from 5.5 % to 8.3 %, which indirectly confirms the model's ability to predict the settling velocity of MP fragments. Second, the irregular fragments and equivalent regular fragments have different settling velocities. That is, even two fragments with identical characteristics, can have different settling velocities, which contradicts the results obtained using the *CSF*-based formula that irregular fragments and regular cuboids have the same settling velocities, indirectly indicating that *CSF* cannot accurately describe the shape of irregular fragments. By comparison, the settling velocity of the fragment A undergoing stable settling is relatively close to that of the equivalent regular rectangular prism (a 17.3 % difference), whereas the fragment B undergoing transitional settling and the fragment C undergoing oscillating settling have considerably different velocities from the equivalent regular rectangular cuboids (differences of 38.2 % and 32.4 %, respectively). This result also reflects the influence of secondary motion on the settling velocity and that using the *CSF* may result in an overestimate of the settling velocity.

More generally, we presented a comparison of the settling velocities and the predicted settling velocities of formulas (Table 5) which are presented for microplastics with various shapes (Francalanci et al., 2021; Waldschlager and Schuttrumpf, 2019; Yu et al., 2022) when using *CSF* and *ISF* as shape factors, respectively. Here, the dimensionless particle size D_{n}^* is calculated as:

$$D_{\text{n}}^* = \left(\frac{(\rho_{\text{p}} - \rho_{\text{w}})g}{\rho_{\text{w}} \nu^2} \right)^{1/3} D_{\text{n}} \tag{27}$$

Finally, the settling velocity W_{s} is calculated using the same formula used in the previous study explicitly (Waldschlager and Schuttrumpf, 2019; Yu et al., 2022):

$$W_{\text{s}} = \sqrt{\frac{4}{3} \frac{g D_{\text{n}}}{C_{\text{D}}} \frac{\rho_{\text{p}} - \rho}{\rho}} \tag{28}$$

Table 4

Predicting settling velocity of irregular fragments A, B, C and equivalent regular cuboids A_{cuboid}, B_{cuboid}, C_{cuboid} using CSF and ISF as shape factors respectively. The Values of prediction are calculated by the formula presented by Yu et al. (2022).

Fragment	A_{cuboid}	B_{cuboid}	C_{cuboid}	A	B	C
Settling velocity (cm/s)	3.16	5.21	5.16	2.63	3.23	3.50
CSF-based prediction (cm/s)	2.96	4.82	4.73	2.96	4.63	4.56
ISF-based prediction (cm/s)	2.96	4.82	4.73	2.49	3.59	3.38

Fig. 13 shows that replacing the *CSF* in the formulas from the literature by the *ISF* improves the predicted settling velocity. This result is unexpected yet reasonable because using the *ISF* transforms the original three-dimensional irregular fragments into three-dimensional regular particles with a uniform short-axis height (h). This transformation can be applied to most formulas for the MP settling velocity. The large error obtained using the formula of (Francalanci et al., 2021) probably results from the irregular MP particles used to obtain their dataset actually being two-dimensional and approximately thin sheet-like particles.

4.3. Formula for the settling velocity of irregularly shaped MP fragments

Although the *ISF* can improve the predictive ability of existing formulas for the settling velocity of irregular MP fragments, these formulas were not developed for irregular MP fragments. Therefore, a new formula was developed in this study for the settling velocity of irregular MP fragments by using settling velocity data. The terminal settling velocity of irregular microplastics is shown in Fig. 14. The Reynolds number of most of the MP fragments are in the transitional range ($1 < Re < 10^3$). The maximum and minimum Reynolds numbers of the MP fragments are approximately 400, and 0.99 (close to the laminar regime), respectively.

The settling velocity data was used to derive a relationship between the drag coefficient C_{D} and the Reynolds number Re of the MP fragments. Fig. 15 shows that C_{D} decreases as Re increases, but the rate of decrease gradually becomes smaller. The relationship between C_{D} and Re can be represented by the following exponential function:

$$ln(C_{\text{D}}) = 3.5 \times Re^{-0.347} + 0.24 \tag{29}$$

As Re approaches infinity, ln(C_{D}) converges to a value of 0.24, which means C_{D} converges to 1.27, close to the experimental results (the average value of C_{D} is 1.24) of (Goral et al., 2023) for various MPs with regular shapes like rectangle prism and tetrahedron which have sharp edges. This phenomenon aligns with classical fluid theory: when the Reynolds number is very large, the fluid flow exhibits turbulent characteristics. In this scenario, the drag coefficient becomes relatively stable, approaching a constant value. This indicates that, in the high Reynolds number regime, the drag on the particle is no longer significantly dependent on the fluid's viscous properties but is instead dominated more by the inertial forces of the fluid. In simpler terms, when the fluid velocity is sufficiently high, the drag on the particle tends toward a stable value, and further increases in velocity do not significantly affect the drag coefficient.

So far, an implicit Eq.(29) for calculating the settling velocity of irregular fragments has been presented. In Eq. (29), only the effects of the density ρ_{p} and size D_{n} on the settling velocity of irregular fragments are considered. To improve the usability of the formula and consider the influence of the irregular shape factor *ISF*, an explicit form of this formula is derived from the original relationship between $C_{\text{D}} \sim f\,(Re)$ and $C_{\text{D}} \sim f\,(D_n^*, ISF)$. Considering that C_{D} is mainly determined by D_n^*, the relationship between $Re \sim f\,(D_n^*)$ and $C_{\text{D}} \sim f\,(D_n^*)$ is derived first, and the influence of the *ISF* is then incorporated as a correction to $C_{\text{D}} \sim f\,(D_n^*)$. Fig. 16 shows the relationship between Re and D_n^*, where ln(Re) exhibits a strong exponential dependence on D_n^*:

$$ln(Re) = 5.6 - 5.8 \times e^{-0.07D^*} \tag{30}$$

Substituting Eq. (30) into Eq. (29) yields the relationship between C_{D} and D_n^*:

$$ln\left(C_{\text{D,without}ISF}\right) = 3.5 \times e^{-1.943+2.01\times e^{-0.07D^*}} + 0.24 \tag{31}$$

To demonstrate how using the *ISF* produces an improved prediction (Eq. (31)), the relationship between the *ISF* and the difference in C_{D} is

Table 5
Formulas for the terminal velocity for MPs with various shapes from the literatures.

Source	Particle	D_n (cm)	ρ_p (g/cm^3)	Re_N	Settling velocity formula
(Yu et al., 2022)	MP	(0.0256, 0.3555)	(1.05, 1.56)	(1, 285)	$W_s = \sqrt{\dfrac{4gD_n(\rho_p-\rho)\left(\left(D_n^*\right)^{-0.25}\psi^{0.03\left(D_n^*\right)}CSF^{0.33\left(D_n^*\right)}\right)^{0.25}}{3\rho\left(\dfrac{432\left(1+0.22\left(D_n^*\right)^3\right)^{0.54}}{\left(D_n^*\right)^3}+0.47\left[1-\exp\left(-0.15\left(D_n^*\right)^{0.45}\right)\right]\right)}}$
(Francalanci et al., 2021)	MP	(0.1678, 0.5441)	(1.03, 1.37)	(76,746)	$W_* = \dfrac{\left(D_n^*\right)^2}{18\left[a\left(\dfrac{a^2+b^2+c^2}{3}\right)^{-1/2}\right]^{-0.38}+\left(0.2781^*CSF^{-0.1602^*}\left(D_n^*\right)^3\right)^{0.4942^*CSF^{-0.059}}}$
(Waldschlager and Schuttrumpf, 2019)	MP	(0.04, 0.5)	(1.00, 1.368)	/	$W_s = \sqrt{\dfrac{4gD_n(\rho_p-\rho)\cdot CSF\cdot\sqrt[3]{Re}}{9\rho}}$

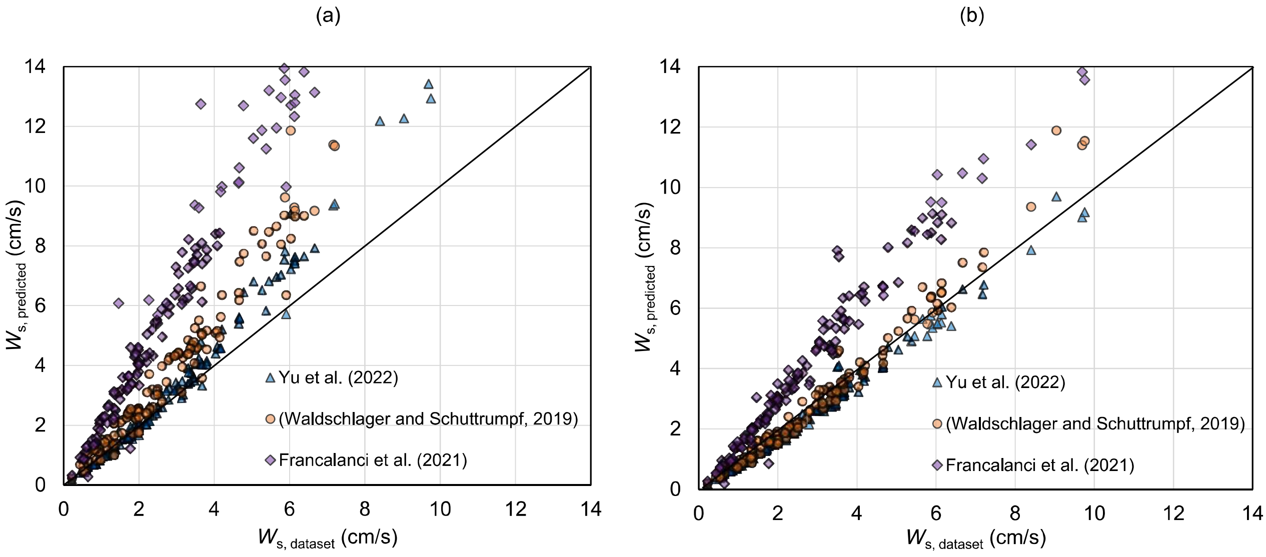

Fig. 13. Predicted settling velocity of irregular MP fragments using the (a) *CSF* and (b) *ISF*.

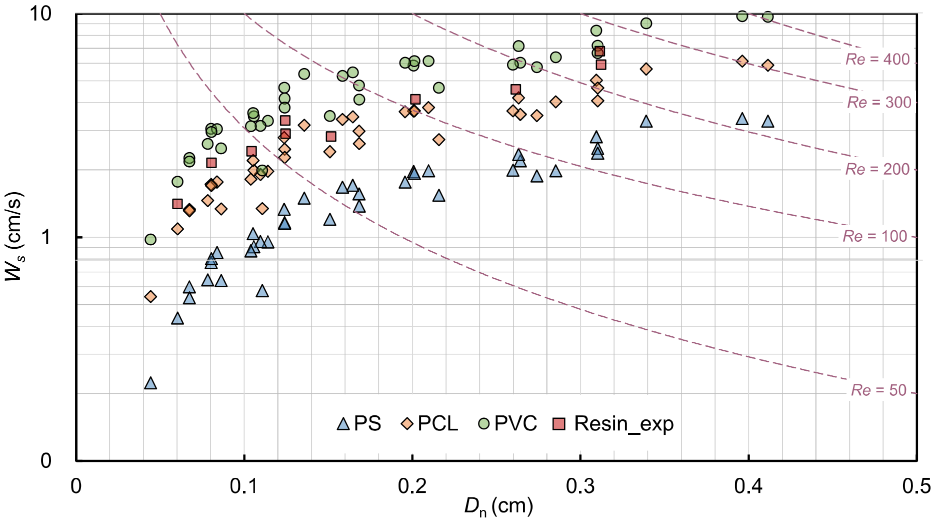

Fig. 14. The settling velocities versus particle size relationship for MP fragments of different polymer types (densities).

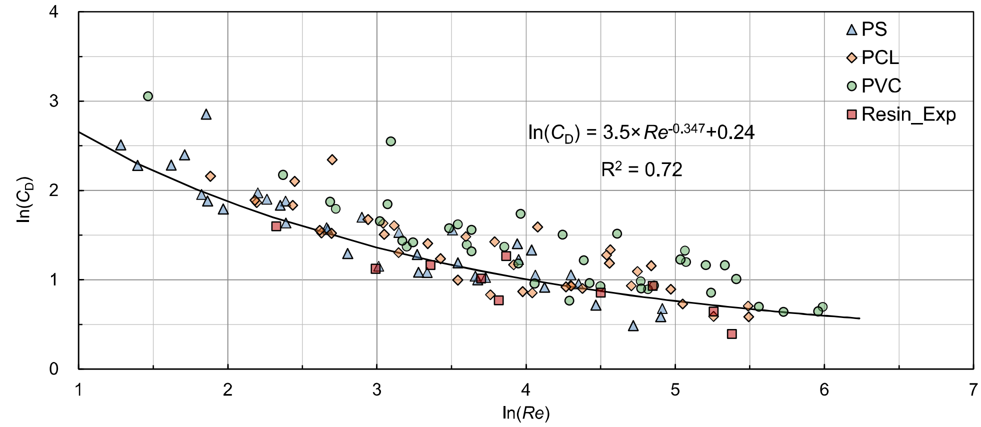

Fig. 15. The relationship between the drag coefficient C_D and Reynolds number Re.

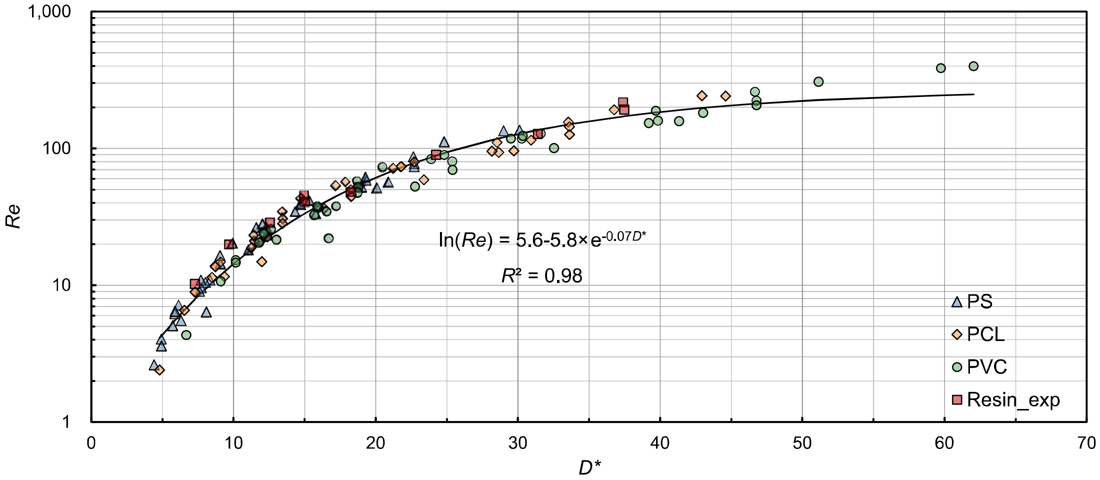

Fig. 16. Relationship between Re and D_n^*.

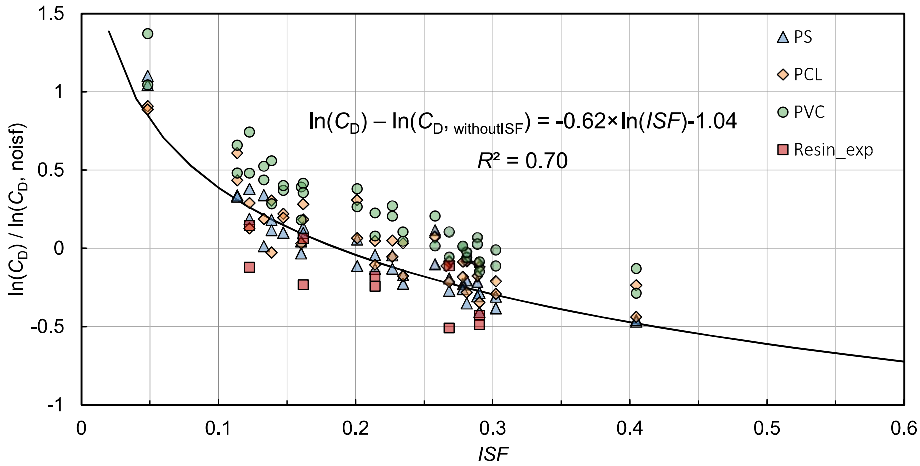

Fig. 17. Relationship between C_D and ISF

shown in Fig. 17. The predicted C_D is overestimated for MP fragments with a large ISF and underestimated for MP fragments with a small ISF. The following logarithmic relationship can be derived:

$$ln(C_D) = ln(C_{D,withoutISF}) - 0.62 \times ln(ISF) - 1.04 \tag{32}$$

Substituting Eq. (32) into Eq. (31) yields the final explicit formula for C_D of irregular MP fragments:

$$ln(C_D) = 3.5 \times e^{-1.943+2.01\times e^{-0.07D^*}} - 0.62 \times ln(ISF) - 0.8 \tag{33}$$

Take Eq. (33) into Eq.(28), an explicit formula for settling velocity of irregular shaped MP fragments can be derived finally:

$$W_s = \sqrt{\frac{4gD_n(\rho_p - \rho)}{3\rho exp\left(3.5 \times e^{-1.943+2.01\times e^{-0.07D^*}} - 0.62 \times ln(ISF) - 0.8\right)}} \quad (34)$$

where exp. presents the exponential function based on the natural number e.

In Section 4.2, the improvement in accuracy when using existing microplastic formulas with *ISF* has been discussed. Furthermore, this section compared the formula proposed with existing formulas in Table 5. The selected formulas include those applicable to microplastics of various shapes (Francalanci et al., 2021; Waldschlager and Schuttrumpf, 2019; Yu et al., 2022). Although few machine learning algorithms can provide formulas, considering the excellent predicting performance of machine learning in recent years, the proposed formula is also compared with several machine learning algorithms known for strong regression and prediction capabilities, including support vector regression (SVR) (Cortes and Vapnik, 1995), the random forest (RF) model (Breiman, 2001), and the convolutional neural network (CNN) model (Gu et al., 2018). The parameter settings and results for the machine learning algorithms are provided in the Supplementary File and Supplementary Data.

Fig. 18 compares the settling velocity predicted using the proposed formula for irregular MP fragments with those predicted by existing formulas for various shapes of microplastics and machine learning algorithms. Using the *ISF* as the shape factor in formulas specifically designed for microplastics (Waldschlager and Schuttrumpf, 2019; Yu et al., 2022) results in higher accuracy than using sediment formulas for predicting the settling velocity of MP fragments. A possible reason for the larger particle sizes predicted by the formula of (Francalanci et al., 2021) compared to those studied in this paper could be that the particles conforming to the fragment shapes in their study have smoother surfaces and higher sphericities, whereas the particles investigated in this study all exhibit distinct angular boundaries. Furthermore, a total of 216 particles in the dataset of (Yu et al., 2022) were classified as having "angular" characteristics, which could potentially explain why the results of his formula are close to those of the present study. The proposed formula exhibits good predictive performance (*MAPE* = 8.1 %, *RMSE* = 0.47 and $R^2 = 0.98$), outperforming existing formulas and achieving the same level of accuracy and fit as the SVR algorithm (*MAPE* = 10.1 %, *RMSE* = 0.27 and $R^2 = 0.98$).

In addition, considering that *ISF* can be difficult to calculate in many situations, we validated the performance of the proposed formula using only *CSF* across other datasets. Fig. 19 shows the performance of various formulas in predicting the settling velocities of MP fragments, with experimental data sourced from the study of (Kowalski et al., 2016). As shown, the presented formula demonstrates good universality, most of the data points fall within the 30 % error margin. The *RMSE* of the formula presented in this paper is 1.35, which is lower than that of formula of (Yu et al., 2022), which incorporates the dataset of (Kowalski et al., 2016), and its performance is comparable to the formula of (Waldschlager and Schuttrumpf, 2019) (*RMSE* = 1.62).

The object of this study is MP particles with irregular shapes, which are classified as fragments based on their shape, especially those with distinct edge angles and polyhedral shapes. Compared to the irregular MP fragments discussed in this paper, regular microplastic particles are less prone to secondary motion. Furthermore, particles with high degrees of roundness and smooth surfaces experience less resistance from water, potentially resulting in a lower drag coefficient than irregular fragments. In addition, there is a certain proportion of micron-sized microplastics in natural water environments such as the ocean, which are more difficult to collect and measure, have a lower settling velocity, and persist in the water column for a longer period of time. Finally, the influence of turbulence in real water bodies on sedimentation cannot be ignored, as turbulence intensity affects the settling velocity and resuspension of particles and decide whether resuspension will occur (Mancini et al., 2024).

5. Conclusions

In this study, a comprehensive investigation of the settling behavior of various irregularly shaped MP fragments in still water was conducted using numerical simulations and physical experiments. The irregular MP fragments were categorized as undergoing three types of settling on the

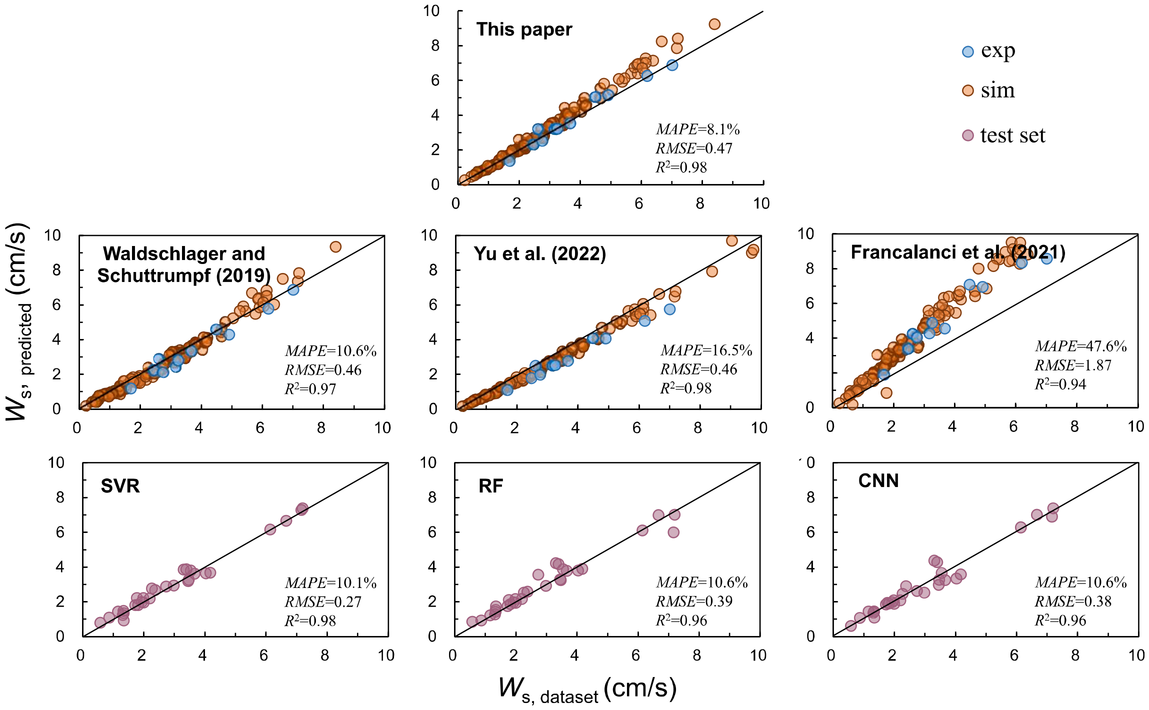

Fig. 18. Comparison between the settling velocities of irregular MP fragments calculated using the proposed formula, existing formulas for various microplastics, and machine learning algorithms. The ratio of the number of training and testing sets used for the machine learning algorithms is 75 %:25 %.

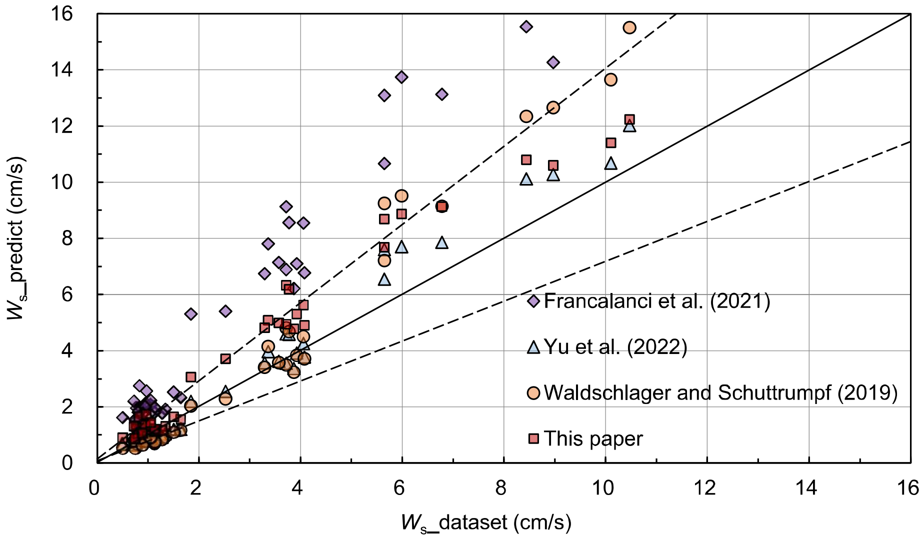

Fig. 19. When applied to other experimental dataset, the performance of each formula.

basis of their secondary motion: stable, transitional, and oscillating. The MP fragments with three-dimensional geometric features tended to undergo oscillating settling, where the settling velocity fluctuated intermittently around the terminal value. By contrast, MP fragments whose longest axes are significantly longer than the intermediate and shortest axes tended to undergo stable settling, where the settling velocity converged to the terminal value.

Although computer programs can be designed to generate MP fragments with specific shapes, one challenge in applying the proposed *ISF* to experimental data is accurately determining the maximum projected area (A_{project}) and the equivalent height (h). More precise and complex techniques, such as image analysis and computer vision, may be needed to model highly irregular and small MP fragments in natural environments.

The research in this paper aims to help better predict the sources, sinks, and migration pathways of microplastics in natural water bodies such as estuaries and oceans. Future improvements in large-scale ocean migration models may help reduce the abundance and hazards of microplastics.

CRediT authorship contribution statement

Chaoqun Ji: Writing – review & editing, Writing – original draft, Visualization, Validation, Software, Methodology, Investigation, Formal analysis, Data curation, Conceptualization. **Jinfeng Zhang:** Visualization, Validation, Supervision, Funding acquisition, Conceptualization. **Guangwei Liu:** Validation, Software, Methodology, Funding acquisition. **Qinghe Zhang:** Supervision, Project administration, Methodology. **Xiaoteng Shen:** Supervision, Methodology.

Declaration of competing interest

The authors declare that they have no known competing financial interests or personal relationships that could have appeared to influence the work reported in this paper.

Acknowledgements

This study was supported by the National Natural Science Foundation of China (Grant No. 52271289), and the National Natural Science Foundation of China (Grant No. 52301335).

Appendix A. Supplementary data

Supplementary data to this article can be found online at https://doi.org/10.1016/j.scitotenv.2024.176857.

Data availability

Data will be made available on request.

References

Breiman, L., 2001. Random forests. Mach. Learn. 45, 5–32. https://doi.org/10.1023/A:1010933404324.

Choi, C.E., Zhang, J., Liang, Z., 2022. Towards realistic predictions of microplastic fiber transport in aquatic environments: secondary motions. Water Res. 218, 118476. https://doi.org/10.1016/j.watres.2022.118476.

Chubarenko, I., Bagaev, A., Zobkov, M., Esiukova, E., 2016. On some physical and dynamical properties of microplastic particles in marine environment. Mar. Pollut. Bull. 108, 105–112. https://doi.org/10.1016/j.marpolbul.2016.04.048.

Cortes, C., Vapnik, V., 1995. Support-vector networks. Mach. Learn. 20, 273–297. https://doi.org/10.1007/BF00994018.

DiBenedetto, M.H., Koseff, J.R., Ouellette, N.T., 2019. Orientation dynamics of nonspherical particles under surface gravity waves. Phys. Rev. Fluids. 4. https://doi.org/10.1103/PhysRevFluids.4.034301.

Fazey, F.M., Ryan, P.G., 2016. Biofouling on buoyant marine plastics: an experimental study into the effect of size on surface longevity. Environ. Pollut. 210, 354–360. https://doi.org/10.1016/j.envpol.2016.01.026.

Francalanci, S., Paris, E., Solari, L., 2021. On the prediction of settling velocity for plastic particles of different shapes. Environ. Pollut. 290, 118068. https://doi.org/10.1016/j.envpol.2021.118068.

Goral, K.D., Guler, H.G., Larsen, B.E., Carstensen, S., Christensen, E.D., Kerpen, N.B., et al., 2023. Settling velocity of microplastic particles having regular and irregular shapes. Environ. Res. 228, 115783. https://doi.org/10.1016/j.envres.2023.115783.

Gray, A.D., Wertz, H., Leads, R.R., Weinstein, J.E., 2018. Microplastic in two South Carolina estuaries: occurrence, distribution, and composition. Mar. Pollut. Bull. 128, 223–233. https://doi.org/10.1016/j.marpolbul.2018.01.030.

Gu, J., Wang, Z., Kuen, J., Ma, L., Shahroudy, A., Shuai, B., et al., 2018. Recent advances in convolutional neural networks. Pattern Recogn. 77, 354–377.

Guo, Z., Zheng, C., Shi, B., 2002. Discrete lattice effects on the forcing term in the lattice Boltzmann method. Phys. Rev. E Stat. Nonlin. Soft Matter Phys. 65, 046308. https://doi.org/10.1103/PhysRevE.65.046308.

Isobe, A., Kubo, K., Tamura, Y., Kako, S., Nakashima, E., Fujii, N., 2014. Selective transport of microplastics and mesoplastics by drifting in coastal waters. Mar. Pollut. Bull. 89, 324–330. https://doi.org/10.1016/j.marpolbul.2014.09.041.

Iwasaki, S., Isobe, A., Kako, S., Uchida, K., Tokai, T., 2017. Fate of microplastics and mesoplastics carried by surface currents and wind waves: a numerical model approach in the sea of Japan. Mar. Pollut. Bull. 121, 85–96. https://doi.org/10.1016/j.marpolbul.2017.05.057.

Jalon-Rojas, I., Wang, X.H., Fredj, E., 2019. A 3D numerical model to track marine plastic debris (TrackMPD): sensitivity of microplastic trajectories and fates to particle dynamical properties and physical processes. Mar. Pollut. Bull. 141, 256–272. https://doi.org/10.1016/j.marpolbul.2019.02.052.

Jalon-Rojas, I., Romero-Ramirez, A., Fauquembergue, K., Rossignol, L., Cachot, J., Sous, D., et al., 2022. Effects of biofilms and particle physical properties on the rising and settling velocities of microplastic fibers and sheets. Environ. Sci. Technol. 56, 8114–8123. https://doi.org/10.1021/acs.est.2c01302.

Ji, C., Zhang, J., Liu, G., Zhang, Q., Xing, E., 2024. Towards better predicting the settling velocity of film-shaped microplastics based on experiment and simulation data. Mar. Pollut. Bull. 203, 116493. https://doi.org/10.1016/j.marpolbul.2024.116493.

Khatmullina, L., Chubarenko, I., 2021. Thin synthetic fibers sinking in still and convectively mixing water: laboratory experiments and projection to oceanic environment. Environ. Pollut. 288, 117714. https://doi.org/10.1016/j.envpol.2021.117714.

Khatmullina, L., Isachenko, I., 2017. Settling velocity of microplastic particles of regular shapes. Mar. Pollut. Bull. 114, 871–880. https://doi.org/10.1016/j.marpolbul.2016.11.024.

Koelmans, A.A., Bakir, A., Burton, G.A., Janssen, C.R., 2016. Microplastic as a vector for Chemicals in the Aquatic Environment: critical review and model-supported reinterpretation of empirical studies. Environ. Sci. Technol. 50, 3315–3326. https://doi.org/10.1021/acs.est.5b06069.

Kooi, M., Nes, E.H.V., Scheffer, M., Koelmans, A.A., 2017. Ups and downs in the ocean: effects of biofouling on vertical transport of microplastics. Environ. Sci. Technol. 51, 7963–7971. https://doi.org/10.1021/acs.est.6b04702.

Kowalski, N., Reichardt, A.M., Waniek, J.J., 2016. Sinking rates of microplastics and potential implications of their alteration by physical, biological, and chemical factors. Mar. Pollut. Bull. 109, 310–319. https://doi.org/10.1016/j.marpolbul.2016.05.064.

Lallemand, P., Luo, L.-S., Krafczyk, M., Yong, W.-A., 2021. The lattice Boltzmann method for nearly incompressible flows. J. Comput. Phys. 431. https://doi.org/10.1016/j.jcp.2020.109713.

Larsen, B.E., Al-Obaidi, M.A.A., Guler, H.G., Carstensen, S., Goral, K.D., Christensen, E. D., et al., 2023. Experimental investigation on the nearshore transport of buoyant microplastic particles. Mar. Pollut. Bull. 187, 114610. https://doi.org/10.1016/j.marpolbul.2023.114610.

Laursen, S.N., Fruergaard, M., Andersen, T.J., 2022. Rapid flocculation and settling of positively buoyant microplastic and fine-grained sediment in natural seawater. Mar. Pollut. Bull. 178, 113619. https://doi.org/10.1016/j.marpolbul.2022.113619.

Lenain, L., Pizzo, N., Melville, W.K., 2019. Laboratory studies of Lagrangian transport by breaking surface waves. J. Fluid Mech. 876. https://doi.org/10.1017/jfm.2019.544.

Maliwan, T., Pungrasmi, W., Lohwacharin, J., 2021. Effects of microplastic accumulation on floc characteristics and fouling behavior in a membrane bioreactor. J. Hazard. Mater. 411, 124991. https://doi.org/10.1016/j.jhazmat.2020.124991.

Mancini, M., Serra, T., Colomer, J., Solari, L., 2023. Suspended sediments mediate microplastic sedimentation in unidirectional flows. Sci. Total Environ. 890, 164363. https://doi.org/10.1016/j.scitotenv.2023.164363.

Mancini, M., Colomer, J., Solari, L., Serra, T., 2024. Shear induced remobilization of buried synthetic microfibers. Environ. Pollut. 361, 124864. https://doi.org/10.1016/j.envpol.2024.124864.

Moreira, F.T., Balthazar-Silva, D., Barbosa, L., Turra, A., 2016. Revealing accumulation zones of plastic pellets in sandy beaches. Environ. Pollut. 218, 313–321. https://doi.org/10.1016/j.envpol.2016.07.006.

Nguyen, T.H., Kieu-Le, T.C., Tang, F.H.M., Maggi, F., 2022. Controlling factors of microplastic fibre settling through a water column. Sci. Total Environ. 838, 156011. https://doi.org/10.1016/j.scitotenv.2022.156011.

Qian, S., Qiao, X., Zhang, W., Yu, Z., Dong, S., Feng, J., 2024. Machine learning-based prediction for settling velocity of microplastics with various shapes. Water Res. 249, 121001. https://doi.org/10.1016/j.watres.2023.121001.

Ryan, P.G., 2015. A brief history of marine litter research. Marine anthropogenic litter. 1–25.

Shamskhany, A., Karimpour, S., 2022. Entrainment and vertical mixing of aquatic microplastics in turbulent flow: the coupled role of particle size and density. Mar. Pollut. Bull. 184, 114160. https://doi.org/10.1016/j.marpolbul.2022.114160.

Song, Y.K., Hong, S.H., Jang, M., Kang, J.-H., Kwon, O.Y., Han, G.M., et al., 2014. Large accumulation of Micro-sized synthetic polymer particles in the sea surface microlayer. Environ. Sci. Technol. 48, 9014–9021. https://doi.org/10.1021/es501757s.

Van Melkebeke, M., Janssen, C., De Meester, S., 2020. Characteristics and sinking behavior of typical microplastics including the potential effect of biofouling: implications for remediation. Environ. Sci. Technol. 54, 8668–8680. https://doi.org/10.1021/acs.est.9b07378.

Waldschlager, K., Schuttrumpf, H., 2019. Effects of particle properties on the settling and rise velocities of microplastics in freshwater under laboratory conditions. Environ. Sci. Technol. 53, 1958–1966. https://doi.org/10.1021/acs.est.8b06794.

Wang, X., Li, J.-L., Wu, Z., Gao, S.-S., Qiu, R., Deng, L., et al., 2020. CMGC: a CAD to Monte Carlo geometry conversion code. Nucl. Sci. Tech. 31, 82. https://doi.org/10.1007/s41365-020-00793-8.

Wang, Z., Dou, M., Ren, P., Sun, B., Jia, R., Zhou, Y., 2021. Settling velocity of irregularly shaped microplastics under steady and dynamic flow conditions. Environ. Sci. Pollut. Res. Int. 28, 62116–62132. https://doi.org/10.1007/s11356-021-14654-3.

Wu, Z., Zhang, J., Yu, H., 2022. Mesoscopic particulate system assembled from three-dimensional irregular particles. Adv. Powder Technol. 33, 103580. https://doi.org/10.1016/j.apt.2022.103580.

Xue, B., Zhang, L., Li, R., Wang, Y., Guo, J., Yu, K., et al., 2020. Underestimated microplastic pollution derived from fishery activities and “hidden” in deep sediment. Environ. Sci. Technol. 54, 2210–2217. https://doi.org/10.1021/acs.est.9b04850.

Yan, M., Nie, H., Xu, K., He, Y., Hu, Y., Huang, Y., et al., 2019. Microplastic abundance, distribution and composition in the Pearl River along Guangzhou city and Pearl River estuary. China. Chemosphere. 217, 879–886. https://doi.org/10.1016/j.chemosphere.2018.11.093.

Yu, Z., Yang, G., Zhang, W., 2022. A new model for the terminal settling velocity of microplastics. Mar. Pollut. Bull. 176, 113449. https://doi.org/10.1016/j.marpolbul.2022.113449.

Zastawny, M., Mallouppas, G., Zhao, F., van Wachem, B., 2012. Derivation of drag and lift force and torque coefficients for non-spherical particles in flows. Int. J. Multiphase Flow 39, 227–239. https://doi.org/10.1016/j.ijmultiphaseflow.2011.09.004.

Zhang, J., Choi, C.E., 2022. Improved settling velocity for microplastic fibers: a new shape-dependent drag model. Environ. Sci. Technol. 56, 962–973. https://doi.org/10.1021/acs.est.1c06188.

Zhang, J., Ji, C., Liu, G., Zhang, Q., Xing, E., 2023. Settling processes of cylindrical microplastics in quiescent water: a fully resolved numerical simulation study. Mar. Pollut. Bull. 194, 115438. https://doi.org/10.1016/j.marpolbul.2023.115438.

Zhong, H., Chen, S., Lee, C., 2011. Experimental study of freely falling thin disks: transition from planar zigzag to spiral. Phys. Fluids 23. https://doi.org/10.1063/1.3541844.

Zhou, T., Li, H., Li, X., Lange, C.F., Ma, Y., 2023. Feature-based modeling for variable fractal geometry design integrated into CAD system. Adv. Eng. Inform. 57, 23. https://doi.org/10.1016/j.aei.2023.102006.

Zou, M., Yu, B., Feng, Y., Xu, P., 2007. A Monte Carlo method for simulating fractal surfaces. Phys. A 386, 176–186. https://doi.org/10.1016/j.physa.2007.07.058.